Influence of the wind field on the radiance of a marine shallow: evidence from the Caspian Sea*

Genrik S. Karabashev[*]
Marina A. Evdoshenko

[1] P. P. Shirshov Institute of Oceanology
of the Russian Academy of Sciences (IO RAS),
36, Nahimovski prospect, Moscow, Russia, 117997;

e-mail: genkar@mail.ru

[*]corresponding author

Abstract

The influence of the near-water wind field on the radiance of a marine shallow was studied on the basis of daily SeaWiFS ocean colour scanner data and QuickScat scatterometer wind data collected from 1999 to 2004 in the southern Caspian Sea, where the deep basin borders a vast shallow west of the shore of meridional extent. It was found that radiance distributions, clustered by wind rhumbs, exhibited different long-term mean patterns for winds of opposing directions: within the shallow's boundaries, the radiances were about twice as high for winds having an offshore component with reference to the onshore wind conditions. The zonal profile of radiance across the shallow resembled a closed loop whose upper and

---

The complete text of the paper is available at http://www.iopan.gda.pl/oceanologia/

lower branches corresponded to the offshore and onshore winds respectively. The loop was the most pronounced at sites with 10–15 m of water for any wavelength of light, including the red region. On the basis of specific features of the study area, we attributed this pattern to sunlight backscattered from bottom sediments resuspended by bottom compensation currents induced by the offshore winds.

1. Introduction

Optical shallowness implies that the water-leaving radiance L_{wn} of a basin depends both on the optical properties of the water body and on the light backscattered from its bed and/or from bottom sediments resuspended by bottom currents. The latter factors hamper the retrieval of chlorophyll from L_{wn} measured in shallow basins but they can be useful for the remote sensing of near-bottom water flows (Karabashev et al. 2009).

The thickness of the layer from which radiance originates

$$Z_{or}(\lambda) = 1/K_d(\lambda)\,, \tag{1}$$

where $K_d(\lambda)$ is the coefficient of daylight attenuation in water at a wavelength λ (Gordon & McCluney 1975). K_d at $\lambda = 470$ nm ranges from 0.02 m^{-1} in oligotrophic waters to 1 m^{-1} or higher in ultra-eutrophic ocean areas or inland seas. Hence, an optically shallow aquatic area can be as deep as 50 m. The remote sensing of such areas has been going on for decades since the beginning of global satellite observations in the microwave, IR and visible ranges. The near-bottom effects can be directly monitored exclusively in the visible since the IR and microwave signals originate at the air-water interface. There are a number of studies dedicated to bottom reflectance and the underwater light field in the context of remote sensing (Boss & Zaneveld 2003, Mobley & Sundman 2003, Kopelevich et al. 2007, and others) but we failed to find experimental evidence for the contribution of light, backscattered by resuspended sediments, to the distribution of radiance in large marine shallows, although sediment resuspension is frequent there and has attracted the attention of many researchers (Demers et al. 1987, Arfi et al. 1993, Booth et al. 2000, Scheffer et al. 2003, and others).

The aim of our study was to come to a tentative conclusion whether a consistent relationship exists between winds of diverse directions and the distribution of the water-leaving radiance in a shallow aquatic area extending for tens of kilometres and more. A further objective of this work was to find out whether the reflectance of the resuspended sediments could be strong enough to dominate the bottom reflectance.

2. Approach, materials and methods

The sea surface layer takes only a few hours to adjust to abrupt changes in wind strength and direction, whereas satellite images are obtained once a day at best. Considerable uncertainty therefore exists concerning the wind field configuration that shapes the distribution of optically-significant seawater admixtures at the instant of flight of a satellite colour scanner. Plausible wind field inhomogeneity is another cause of possible misinterpretation of the relationship between wind conditions and radiance distributions in the satellite images when these are compared on an everyday basis.

We have assumed that these difficulties can be at least partly bypassed if we cluster the images of a shallow area by wind directions at the instants of the survey and use the mean radiance distribution of a cluster to find features characteristic of respective wind conditions. Presumably, the averaging of a well-populated cluster of radiance distributions will result in a mean radiance distribution whose features are more closely related to the respective wind direction thanks to the random nature of the above uncertainty.

Our approach implies the use of the red radiance L_{wnred} at $\lambda > 650$ nm and the reference radiance L_{wnref} at wavelengths of the 'transparency window' (from about 470 nm in the open ocean to 560 nm and more in the least transparent waters (Jerlov 1976)) as guides for distinguishing the effects of the backscattering of light from the resuspended bottom sediments and from the interface between the sea bed and the water thickness (bottom reflectance). The water itself absorbs red light to such an extent that the origination layer of the red water-leaving radiance is universally no more than 2–3 m thick (Figure 1). Hence, at sites with more than 3 m of water, the bottom reflectance contributes nothing to L_{wnred} although the latter remains sensitive to resuspended bottom sediments penetrating the near-surface layer. In other words, the 3 m depth is a universal threshold of red radiance sensitivity to bottom reflection (Figure 1), and the similarity of the horizontal distributions of L_{wnred} and L_{wnref} over the shallow area points to a particularly strong resuspension of bottom sediments, because Z_{or} for L_{wnref} delimits a much thicker surface layer than Z_{or} for L_{wnred} does ($L_{\mathrm{wnref}}/L_{\mathrm{wnred}}$ criterion).

We chose a shallow in the south-eastern Caspian Sea as the study area (Figure 2) because it has the features of a desired natural model: (1) the waters of the South Caspian basin, flowing across the shallow, are fairly transparent (Simonov & Altman 1992), which facilitates observations of resuspension effects; (2) the bed of the shallow is mainly free of sea grass and consists of bare sand, silt and other light-coloured sediments that are
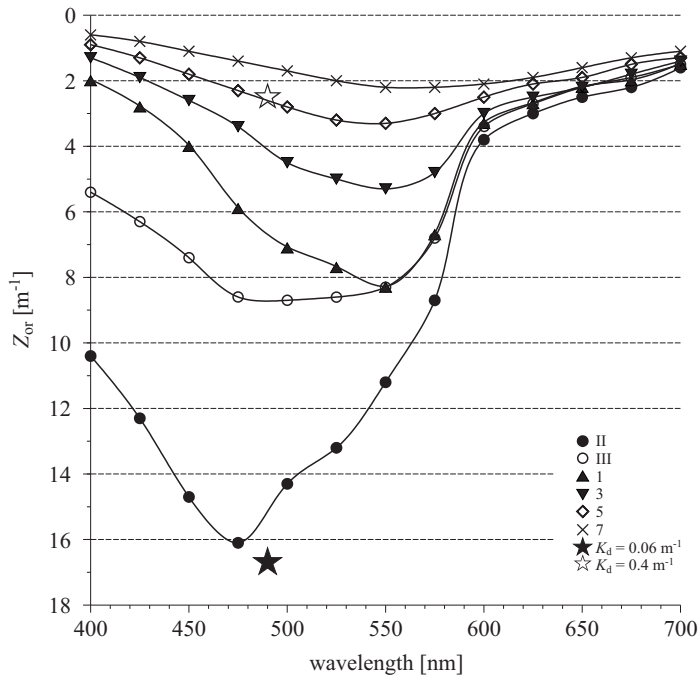
Figure 1. Wavelength dependence of the thickness of the radiance origination layer Z_{or} according to (1) and Jerlov's optical water types II and III (ocean waters) and 1–7 (coastal waters) (Table XXVII in Jerlov 1976). The asterisks indicate Z_{or} at minimum and maximum $K_d(490)$ characteristic of the study area (Figure 2) according to monthly mean distributions computed from MODIS-Aqua data for April–September at http://disc.sci.gsfc.nasa.gov/giovanni/

detachable from the sea floor by quite moderate water motions; (3) digital bottom topography of the Caspian Sea is available online at http://caspi. ru/HTML/025/02/Caspy-30-10.zip (Figure 2b); (4) the shallow extends for about 200 km in latitude and from 40–50 to 110–120 km in longitude and is clearly delimited by the shore line in the east and by an underwater precipice to the west of the 20–30 m depth contours (Figure 2b); (5) only a few rivers with a minor discharge rate enter the south-eastern Caspian Sea, which minimizes the occurrence of externally supplied sediments; (6) the bottom relief is fairly smooth at sites of plausible sediment resuspension (depth range up to 15–20 m, Figure 2b); (7) the south-eastern Caspian Sea is a region where sunny weather prevails.

Our approach implies the use of a long-term data set of the **Sea**-viewing **Wi**de **F**ield-of-view **S**ensor (SeaWiFS), since it is equipped with a sun-glint avoidance facility. Use has been made of archived water-leaving radiance distributions at wavelengths 412, 443, 490, 510, 555 and 670 nm as standard
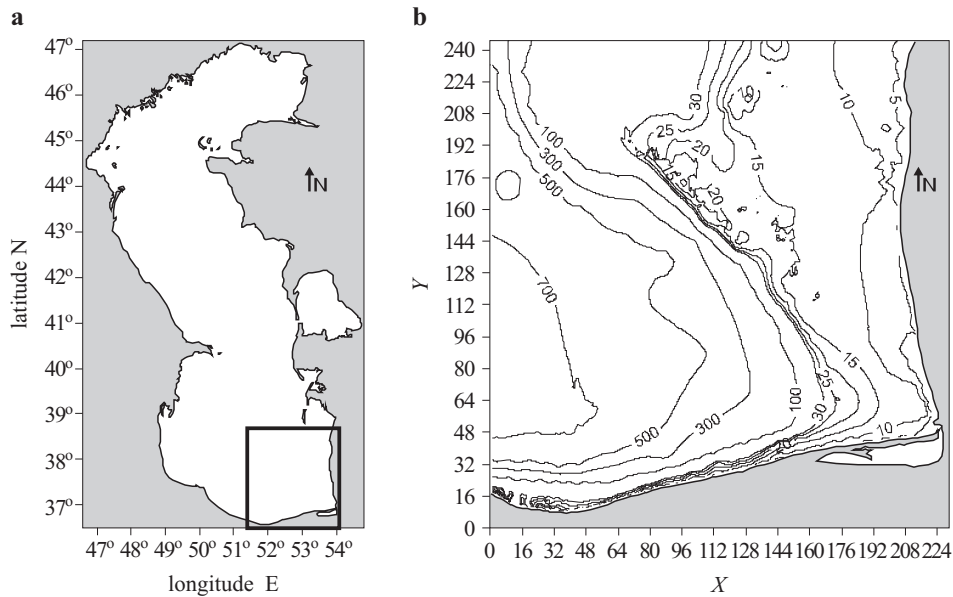
a

b

Figure 2. Location of the study area (heavy-line rectangle) in the Caspian Sea (a) and isobaths of the bottom relief of the area in metres relative to the 27 m sea level plotted from http://caspi.ru/HTML/025/02/Caspy-30-10.zip (b). X and Y [km], are the distances in longitude and latitude from $51°30'$E, $36°30'$N

level L2 products with pixel size 1.1×1.1 km, collected during the NASA global ocean mission in the 1999–2004.

The second data set involves the daily estimates of the near-water before-noon wind vectors obtained at $15'$ spacing with the scatterometer QuickScat in 1999–2004 and available at http://poet.jpl.nasa.gov. We restricted ourselves to eight wind velocity directions with the following designations and mean azimuths φ_i: S-N, $\varphi_1 = 0°$; SW-NE, $\varphi_2 = 45°$; W-E, $\varphi_3 = 90°$; NW-SE, $\varphi_4 = 135°$; N-S, $\varphi_5 = 180°$; NE-SW, $\varphi_6 = 225°$; E-W, $\varphi_7 = 270°$; SE-NW, $\varphi_8 = 315°$. Any wind vector in the range $\varphi_i \pm 22°30'$ was assigned to the i-th direction.

The SeaWiFS and QuickScat data and the bottom bathymetry were displayed for every year day (YD) as superimposed maps of the testing area (Figure 2). The data of a YD were regarded as acceptable if (a) the valid wind estimates made up at least 50% of their possible number within the testing area; (b) $V > 3$ m s^{-1}, where V is the wind speed averaged over the testing area; (c) there were no mesoscale radiance extrema extending over the area (for instance, occasional east-bound plumes from the nearest river mouths crossing the 20–30 m isobaths). We neglected the YDs with wind vectors not exhibiting any dominant direction. The wind data for

selected YDs were clustered by the above azimuths φ_{1-8}, and respective subsets of radiance data, similar to the wind clusters in the YDs involved, were composed for subsequent analysis. Selection of YDs by wind features resulted in severe shrinking of data. The data volume was additionally reduced when passing from wind clusters to the radiance ones, since the wind data were much more regular than the sea surface images in the visible.

The geographical coordinates of the pixels of the images were converted into linear ones relative to $51°30'$E, $36°30'$N (Figure 2). The pixel radiances of every cluster were averaged over the period from 1999 to 2004 in 4×4 km bins after the removal of outliers based on the three sigma rule. In the case of well-populated clusters, a high statistical significance was typical of the averaged binned radiances $L_{\mathrm{wnav}}(\lambda)$ because they were calculated from samples of 200–300 members. The averaging resulted in geographically identical tables of L_{wnav} for $\lambda = 412, 443, 490, 510, 555$ and 670 nm for each of the eight clusters. These tables were used for visualizing the spatial behaviour of the spectral radiances.

3. Results

The information obtainable from a comparison of radiance distributions of winds from different directions depends on the cluster population. In our case, the number of members N_i of the i-th cluster at wind azimuths $\varphi_{1...8}$ varied as 4, 2, 33, 13, 11, 14, 34 and 5. The most and equally populated clusters ($N_3 = 33$, $\varphi_3 = 90°$) and ($N_7 = 34$, $\varphi_7 = 270°$) correspond to events associated with the onshore and offshore winds (Figure 2b).

Onshore and offshore winds. Figure 3 displays the spatial behaviour of radiances in the blue, green and red ($\lambda = 443, 555$, and 670 nm). For better comparability, we expressed the mean radiance L_{wnb} of a bin at a given wavelength as a fraction of radiance range, common to the offshore and onshore conditions:

$$L_{\mathrm{wnb}}\% = 100 \frac{L_{\mathrm{wnav}} - L_{\mathrm{wnav}}^{\min}}{L_{\mathrm{wnav}}^{\max} - L_{\mathrm{wnav}}^{\min}} , \qquad (2)$$

where $L_{\mathrm{wnav}}^{\max}$ and $L_{\mathrm{wnav}}^{\min}$ are the maximum and minimum radiances of clusters $\varphi_3 = 90°$ and $\varphi_7 = 270$. The radiance of the shallow in Figure 3 substantially exceeds that of the South Caspian basin at any wavelength regardless of winds, but radiance distributions within the shallow's limits exhibit explicit dependences on wind direction and spectral range. The maximum L_{wnb} is located east of the 5 m depth contour. Under the offshore conditions (Figure 3, (a)–(c)), the maximum L_{wnb} occurs closer to the shore, shifts southwards and occupies a smaller area when passing from the blue spectral range to the red one. The same takes place in the case of onshore winds
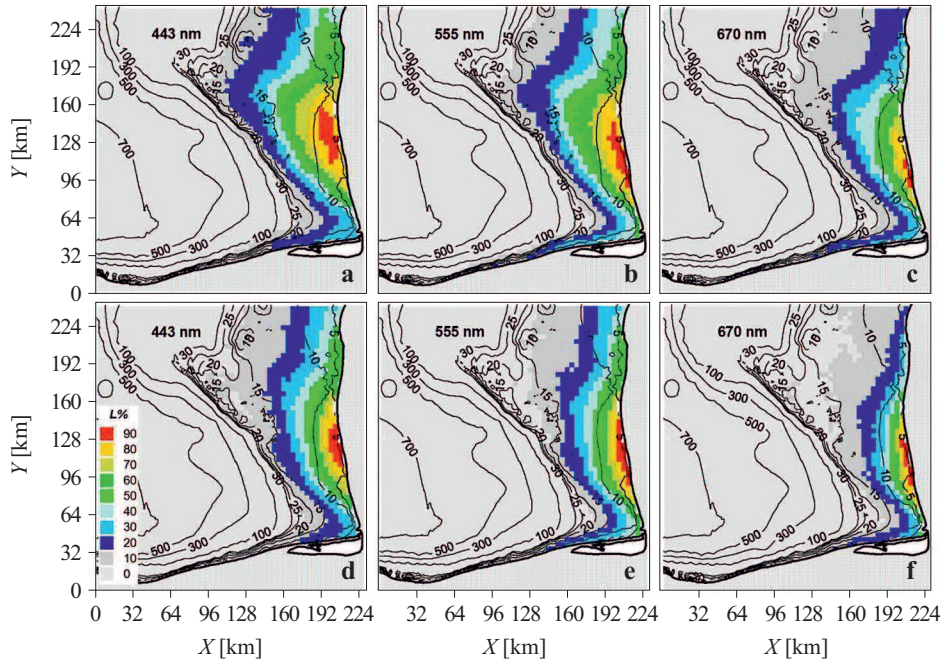
Figure 3. Distributions of the relative long-term mean radiance L_{wnb} at $\lambda = 443$, 555 and 670 nm for offshore (a)–(c) and onshore (d)–(f) winds. X and Y are the distances in longitude and latitude from $51°30'$E, $36°30°$N. See text for details

except for the southward shift of radiance maxima (Figure 3, (d)–(f)). The radiances of moderate intensity extend tens of kilometres further westwards in the case of the offshore wind as compared to the onshore one. This difference peaks at latitudes corresponding to $Y \sim 150$–200 km (Figure 3).

The differences $dL_{\text{wnav}}^{\text{off}-\text{on}}(\lambda) = L_{\text{wnav}}^{\text{off}}(\lambda) - L_{\text{wnav}}^{\text{on}}(\lambda)$, where $L_{\text{wnav}}^{\text{off}}(\lambda)$ and $L_{\text{wnav}}^{\text{on}}(\lambda)$ are binned radiances at offshore and onshore winds, are mapped in Figure 4. The maximum $dL_{\text{wnav}}^{\text{off}-\text{on}}(\lambda)$ are comparable to the $L_{\text{wnav}}^{\text{on}}(\lambda)$ in magnitude, are located between the 10 and 15 m isobaths and extend from 90 to 180 km in the y-axis and from 140 to 200 km in the x-axis.

In Figure 5, the zonal profiles of the bottom relief are compared to the profiles of radiance differences dL_{wnav} at 443, 555 and 670 nm. It is evident that (1) dL_{wnav} distributions west of the shallow are flat and exhibit minor between-profile distinctions; (2) profile segments at depths $Z < 30$ m indicate substantial enhancement of $L_{\text{av}}^{\text{off}}(\lambda)$ against $L_{\text{av}}^{\text{on}}(\lambda)$ at sites with moderate steepness of the sea floor (profiles (d)–(g)) and a virtually zero radiance difference at greater bottom steepness (profiles (a) and (b)); (3) profiles of $dL_{\text{av}}(443)$ and $dL_{\text{av}}(555)$ have the highest magnitude and resemble each other in position and shape, but a number of
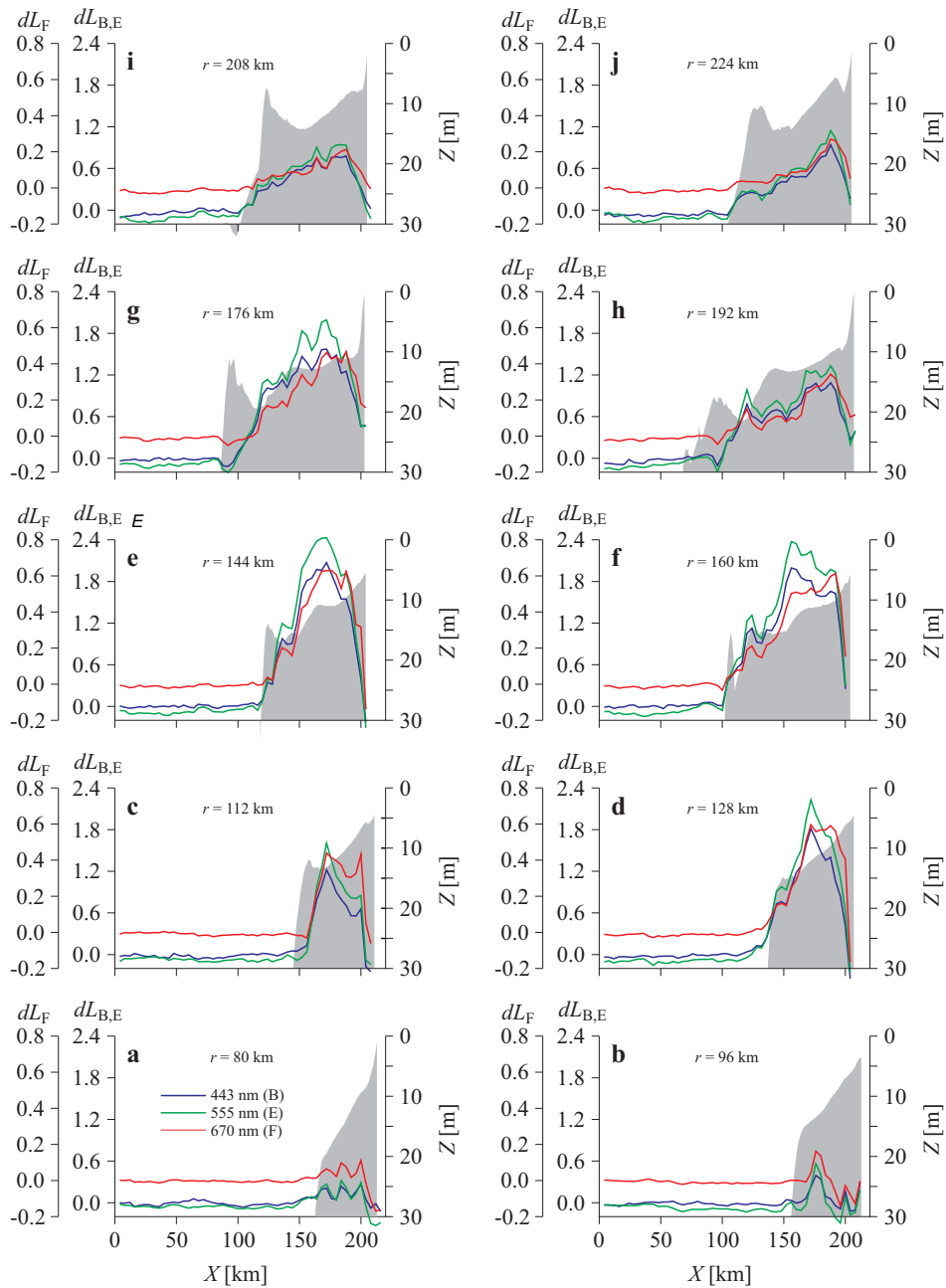
Figure 4. Distributions of the differences $dL_{\text{wnav}}(\lambda)$ in the long-term mean offshore and onshore radiances at 443 (a), 555 (b) and 670 (c) nm. X and Y are the distances in longitude and latitude from 51°30′E, 36°30′N. See text for details

$dL_{\text{av}}(670)$ profiles appear to be shifted eastwards and differ in shape from the corresponding radiance profiles at shorter wavelengths (d)–(f).

The profiles of $L_{\text{av}}^{\text{off}}$ and $L_{\text{av}}^{\text{on}}$ in Figure 6 demonstrate the following trend: the onshore radiance slightly exceeds the offshore radiance in the deep-water part of the middle and northern testing area; an inverse relation between them occurs at the western boundary of the shallow; further east, $L_{\text{av}}^{\text{off}}$ grows faster than $L_{\text{av}}^{\text{on}}$ but the latter overtakes the former in the vicinity of the coastline. As a result, the summary radiance progression in the presence of easterly and westerly winds looks like a closed loop, whose lower and upper branches correspond to the onshore and offshore events. The eastern intersections of the branches occur at sites of less than a few metres of water, where the insufficient accuracy of the bottom topography model prevents a stricter association of intersections with bottom features. The higher-sensitivity profiles in Figure 6 (dashed) indicate that western intersections occurred at $Z > 30$ m if $r <= 160$ km but occurred at sites with 14–30 m of water in profiles at $r > 160$ km distinguished by roughness of bottom relief in the west of the shallow. In some cases the depth and radiance profiles show conformity in their shape: the two-step structures of the offshore branch of the radiance loop and of the bottom profile in Figure 6f appear to be a manifestation of such conformity. However, the more intricate relationships of these profiles outnumber the situations of straightforward interpretability.

Non-zonal winds. The distributions of radiances $L_{\text{wnav}}(555)$ and $L_{\text{wnav}}(670)$ at $\varphi = 180°$ and $\varphi = 0°$, blowing parallel to the shore, demonstrate that both radiances gradually attenuate with distance from the shore (Figure 7, (a)–(d)) as in the case of zonal winds. At the same

Figure 5. Zonal profiles of bottom relief Z [m], (filled contours) and radiance differences $dL_{\mathrm{wnav}}(443)$ (blue, index B), $dL_{\mathrm{wnav}}(555)$ (green, index E) and $dL_{\mathrm{wnav}}(670)$ (red, index F) at latitudes corresponding to Y from 80 to 224 km. r is the distance of profiles (a)–(j) from $36°30'$N (see Figure 2b)
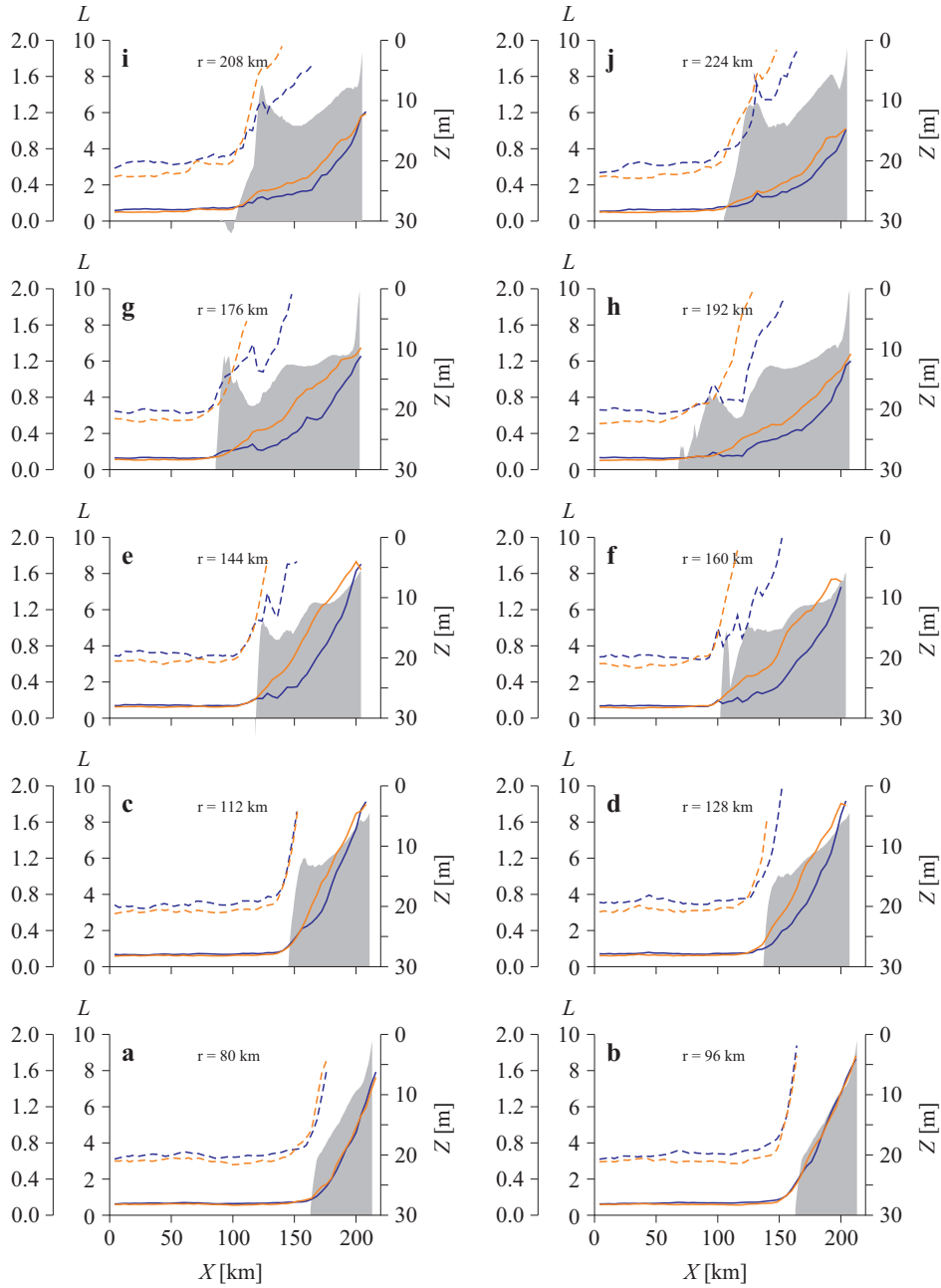
Figure 6. Zonal profiles of bottom relief Z [m], (filled contours) and full-range $(0–10\,\mu\text{W sr}^{-1}\,\text{cm}^{-2}\,\text{nm}^{-1})$ profiles of the offshore $L_{\text{wnav}}^{\text{off}}(555)$ (orange, solid) and onshore $L_{\text{wnav}}^{\text{on}}(555)$ (blue, solid) radiances at latitudes corresponding to Y from 80 to 224 km. r is the distance of profiles (a)–(j) from 51°30′E, 36°30′N (see Figure 2b). The respective dashed curves represent the same profiles in the range $0–2\,\mu\text{W sr}^{-1}\,\text{cm}^{-2}\,\text{nm}^{-1}$

time, a northward shift of these patterns at $\varphi = 0°$ relative to the patterns at $\varphi = 180°$ is distinguishable (compare (a) and (c) with (b) and (d) in Figure 7). The underpopulated radiance cluster at $\varphi = 0°$ is inferior in reliability as against the 11-member cluster at $\varphi = 180°$. We have randomly subdivided the latter into three subclusters of five members each so that any subcluster is comparable to the $\varphi = 0°$ cluster in the population. Presumably, the authenticity of the above shift may be regarded as satisfactory if a radiance profile from the $\varphi = 0°$ data exhibits a maximum shift northwards with reference to any of the $\varphi = 180°$ subclusters. The meridional profiles of radiances $L_{\mathrm{wnav}}(555)$ and $L_{\mathrm{wnav}}(670)$ ((e) and (f) in Figure 7) confirm this supposition. Notice that the profiles of $L_{\mathrm{wnav}}(555)$ and $L_{\mathrm{wnav}}(670)$ for both wind directions peak within the segment of virtually constant depth $Z = 11.1 \pm 0.2$ m (Figure 7).
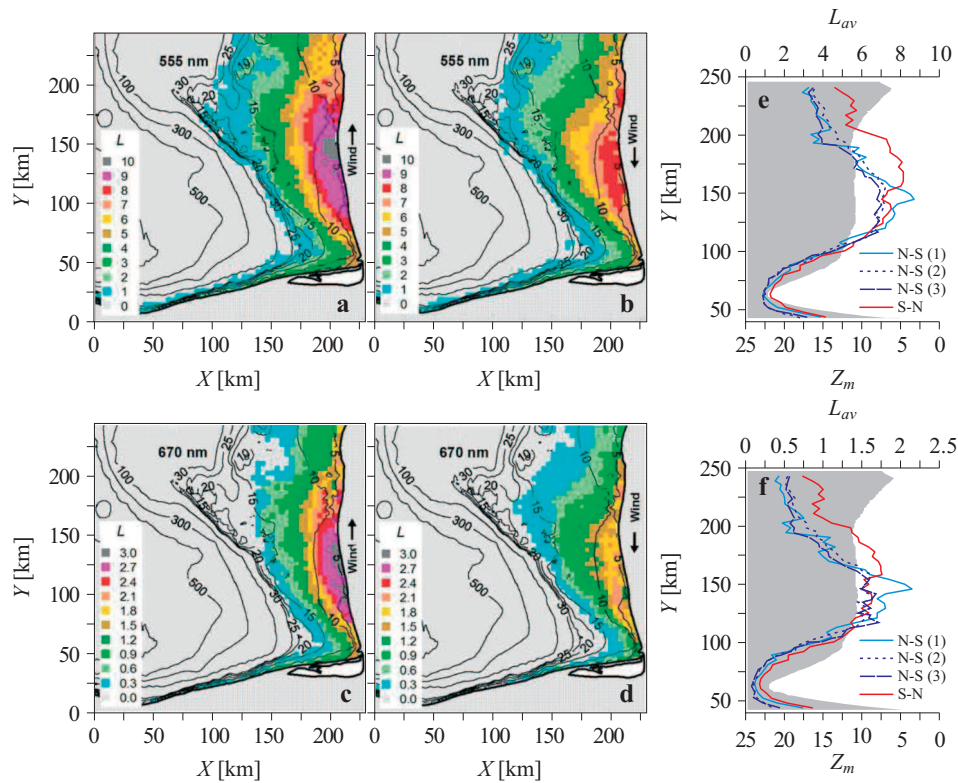

Figure 7. Maps of the study area's bottom relief (depth contours) and distributions of radiances $L_{\mathrm{wnav}}(555)$ and $L_{\mathrm{wnav}}(670)$ for winds of $\varphi = 0°$ ((a) and (c)) and $\varphi = 180°$ ((b) and (d)) and meridional profiles of $L_{\mathrm{wnav}}(555)$ (e) and $L_{\mathrm{wnav}}(670)$ (f) for the same radiances at $X = 180$ km and for winds of $\varphi = 0°$ (S-N, red) and $\varphi = 180°$ (N-S, blue). X and Y are the distances in longitude and latitude from $51°30'$E, $36°30'$N. For details, see text
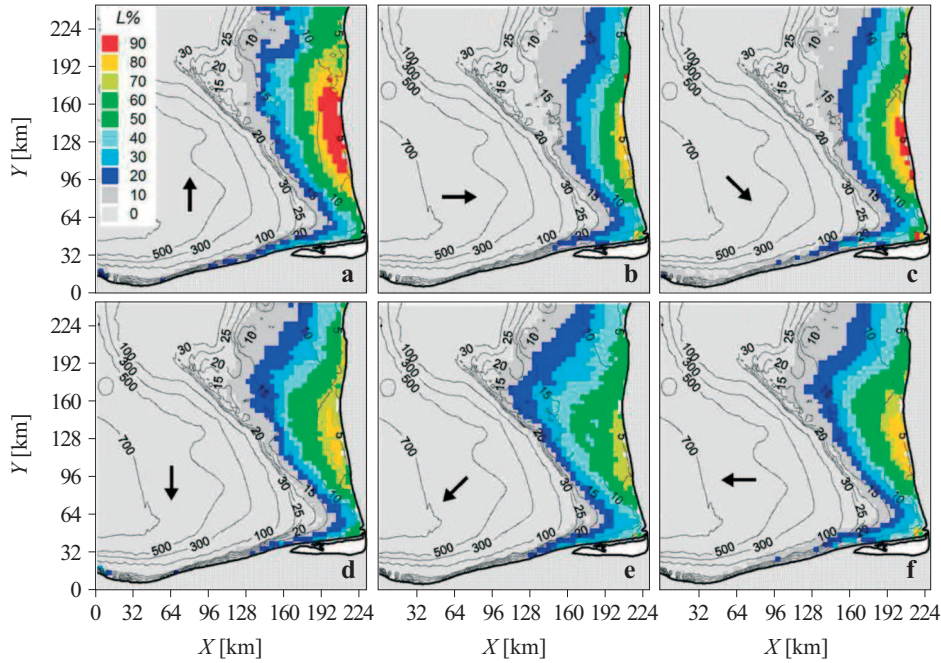
Figure 8. The distributions of the relative mean radiance $L_{wnb}\%$ at $\lambda = 555$ nm for winds of different directions (arrows). X and Y are the distances in longitude and latitude from $51°30'$E, $36°30'$N. For details, see text

All the radiance distributions for winds of different directions are given in Figures 8 and 9, except for the distributions of the two least populated clusters. We consider the radiances at wavelength 555 and 670 nm alone since distributions of L_{wnav} at shorter wavelengths are close to the pattern at 555 nm. For the sake of comparability, we have used (2) to express L_{wnav} as a fraction of the radiance range $L_{wnav}^{max} - L_{wnav}^{min}$, common to all of the wind directions at a given wavelength. They exhibit the following: 1) the maximum $8.30 < L_{wnav}^{max}(555) < 10.41$ μW sr^{-1} cm^{-2} nm^{-1} and $2.34 < L_{wnav}^{max}(670) < 3.20$ μW sr^{-1} cm^{-2} nm^{-1} occurred in the middle of the eastern coastal zone close to the shore line regardless of wind direction; 2) the radiance distributions appear pressed against the shore for winds with an onshore component ((b) and (c) in Figures 8 and 9) but they appear to be extended downwind by 10–15 km if there is an offshore wind component ((e) and (f) in Figures 8 and 9); 3) for one and the same wind involving an offshore component, the green radiance $L_{wnav}(555)$ spreads westwards further than the red radiance $L_{wnav}(670)$ of the same relative magnitude does; 4) winds blowing parallel to the shore result in a meridional rather than a zonal radiance displacement ((a) and (d) in Figures 8 and 9).
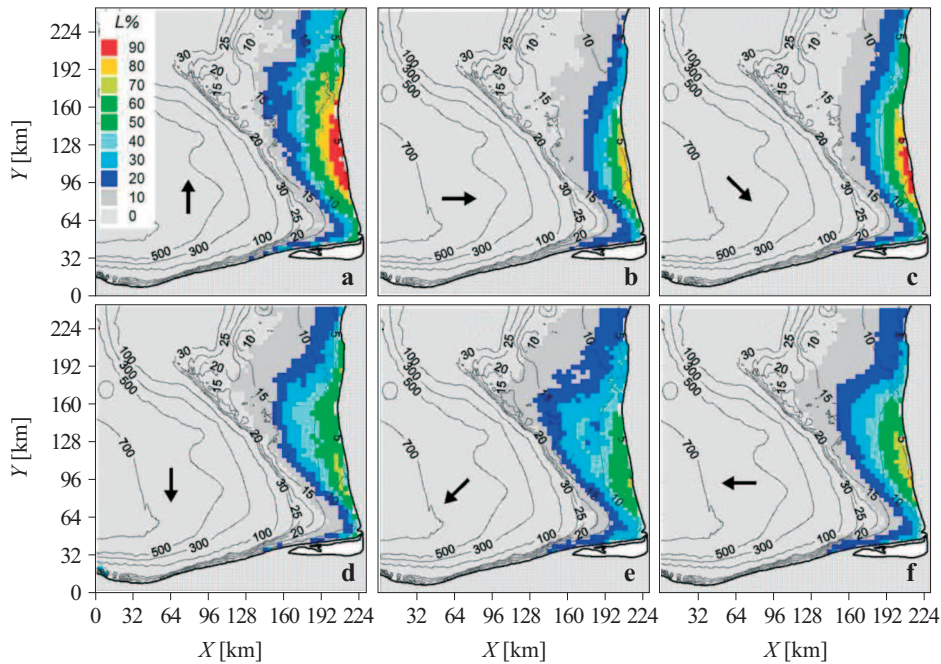
Figure 9. The distributions of the relative mean radiance $L_{\mathrm{wnb}}\%$ at $\lambda = 670$ nm for winds of different directions (arrows). X and Y are the distances in longitude and latitude from $51°30'$E, $36°30'$N. For details, see text

4. Discussion

We found that the estimates of the long-term average normalized radiance of this marine shallow varied to the first significant figure in the middle of the shallow and was spatially redistributed in the direction of moderate long-term average winds, which is manifested as a radiance loop effect for on- and offshore winds. Nothing of this sort happened in the deep-water area only a few km west of the shallow's offshore boundary. These patterns are therefore inherent to the shallow. On the basis of the optical shallowness concept, we examined the sea surface, water-bottom interface and water thickness as conceivable contributors to this effect.

Sea surface. As far as surface waves are concerned, a recent computation for wind speeds as high as 20 m s^{-1} showed that '... the transmittance of the (whitecap-free) air-water interface is nearly identical (within 0.01) to that for a flat interface' (Gordon 2005). The whitecaps are equally probable on both sides of the shallow's offshore boundary (Figure 2), which is inconsistent with the fact that the radiance loop occurred exclusively within the shallow's perimeter. The natural anharmonicity of surface waves may result in a perceptible asymmetry of surface reflectance for opposite

winds. Hypothetically, this mechanism explains the systematic positive bias of $L_{\mathrm{wnav}}^{\mathrm{on}}(555)$ with reference to beyond the shallow, but this bias is much lower than the difference between the branches of the loop inside the shallow (Figure 6). Most likely, the radiance loop effect cannot be attributed to surface wave effects.

Bottom reflectance. Based on the $L_{\mathrm{wnref}}/L_{\mathrm{wnred}}$ criterion, the wavelength dependence of Z_{or} (Figure 1) and the similarity of distributions of the long- and shortwave radiances for winds of similar directions (Figures 3–9), we infer that bottom reflection contributed nothing to the radiance loop effect that took place within the shallow in Figure 2 at sites with more than 5 m of water. In the context of the present work, this inference makes it needless to discuss the reflectance of the shallow's water-bottom interface.

Water thickness. The term 'normalized' suggests that L_{wn} of a deep basin depends exclusively on the backscattering and absorption of light in water (Gordon et al. 1988):

$$L_{\mathrm{wn}}(\lambda) \sim \frac{b_p(\lambda)}{b_p(\lambda) + a(\lambda)}, \tag{3}$$

where $b_p(\lambda)$ and $a(\lambda)$ are the backscattering and absorption coefficients of seawater. Where $b_p(\lambda)$ is concerned, suspended particulate matter (SPM) is the only constituent of light scatterers that matters when dealing with waters of inland seas (specifically, the Caspian Sea), relatively rich in SPM. Any changes in wind conditions resulted in variations of $L_{\mathrm{wn}}(\lambda)$ within the shallow. They were positive with respect to the much lower and quasi-constant $L_{\mathrm{wn}}(\lambda)$ of the neighbouring deep basin. This is also true for $L_{\mathrm{wn}}(670)$, which is not influenced by coloured dissolved organic matter (CDOM), the main factor of the variability of $a(\lambda)$ in natural waters. The irrelevance of bottom- and surface-related factors to the radiance loop effect and other evidence necessitates focusing on the sources that can supply backscattering sediments to the water of the shallow.

There are a number of active mud volcanoes within the shallow's boundaries (Pautov 1959 (ed.)). The largest of them are the Ul'skiy Bank (38°27′N, 52°5′E) and the Griazny Vulkan Bank (38°08′N, 52°33′E). When selecting the images of the testing area for the present study, we found only a few images of the shallow that bear evidence of local radiance maxima appearing to be plausible manifestations of volcanic activity. Such maxima were too insignificant in size and rate of occurrence to affect the long-term radiance distributions.

As is well known, an offshore wind induces coastal water upwelling that brings nutrients into the basin's upper layer, thus creating conditions for

the blooming of phytoplankton with a consequent increase in SPM content in the water. This succession of processes takes several days to produce an excessive sediment concentration. Our approach involves the use of radiance and wind data for one and the same YD, thanks to which the results of data processing cannot be contaminated by the consequences of wind-induced upwelling events, even though they actually did take place.

Uncorrected satellite images of the Caspian Sea show jet-like structures, which are regarded as carriers of dust from the Central Asian deserts. This dust fallout can enhance L_{wn} estimates. The standard atmospheric correction algorithm of colour scanner missions removes the fallout effects from the normalized water-leaving radiance. The low and virtually constant L_{wn} just west of the testing area for any winds in our figures confirm the algorithm's efficiency.

So, there are no grounds for believing that the redistribution of radiance fields within the shallow for moderate winds from different directions was due to factors other than the wind-induced resuspension of bottom sediments. The close resemblance of the distributions of red and shortwave radiances for winds of any direction, including the offshore wind, indicates that the resuspension mechanism fills the water column with resuspended particles up to the near-surface layer. The maximum estimates of radiance difference $dL_{wnav}(\lambda)$ for opposing winds gravitated towards the middle of the shallow with the most gentle bottom slope between the 10 and 15 m isobaths (Figure 4). This and other facts point to the dependence of resuspension efficiency on the wind direction and to the non-uniform distribution of resuspension efficiency over the shallow under a steady wind.

The issue of resuspension efficiency is a typical interdisciplinary problem that involves such lines of inquiry as mesoscale water dynamics, water density stratification, inherent optical properties of water, size spectrum and properties of particles of bottom sediments, the nature of the bottom substrate ranging from sand and mud to a canopy of macrophytes, the impact of bioturbation on the bottom sediments strength etc. This is beyond the scope of the present work. The published evidence, concerning the water dynamics, sedimentology, meteorology and other branches of oceanology for the southern Caspian Sea, is far from matching the long-term satellite observations in volume and regularity. Therefore we have to rely on common knowledge of shallow water conditions when discussing the offshore-onshore radiance loop mechanism.

In the east, the offshore and onshore branches of the loop tend to cross mainly between the 5 m depth contour and the shoreline (Figure 5). There is some uncertainty regarding the location of their crossings with respect to the true local depth due to the insufficient accuracy of the bottom topography

model, sea level instability, and inadequate spatial resolution of radiance data in the near-shore space. In any case, the latter comprises the surf zone. Its radiance peaks during onshore winds when the bottom reflectance radiance is added to the radiance of the water column enhanced by the backscattering of particles resuspended by wave-breaking. The surf zone is virtually free of wave-breaking during offshore winds and, therefore, the dominance of the onshore radiance over the offshore one in the close vicinity of the shoreline is a quite predictable event.

The contribution of bottom reflection to the red radiance vanishes at depths $Z > 3$ m, whereas green radiance can be contributed to by bottom reflection in much deeper waters ((1) and Figure 1). These considerations agree well with the fact that maximum $L_{\mathrm{wnav}}^{\max}(\lambda)$ gravitated to the eastern shores of the testing area regardless of wind direction (Figure 3) and that the maxima of profiles $dL_{\mathrm{av}}(670)$ tend to be shifted shorewards as compared to similar maxima at shorter wavelengths (Figure 5).

The largest positive differences $dL_{\mathrm{wnav}}^{\mathrm{of\_on}}$ in the blue, green and red occurred at depths $10 < Z < 15$ m ((d)–(f) in Figure 5). The spectral-different $dL_{\mathrm{wnav}}^{\mathrm{of\_on}}$ changed concurrently in the zonal direction and occupied one and the same profile segments, where the bottom depth is large enough to prevent the wave-breaking resuspension mechanism. Hence, the difference in sediment resuspension, induced by opposing winds, has to be the only cause of the $dL_{\mathrm{wnav}}^{\mathrm{of\_on}}(670)$ peak. Evidently, the same is true for $dL_{\mathrm{wnav}}^{\mathrm{of\_on}}(555)$ and $dL_{\mathrm{wnav}}^{\mathrm{of\_on}}(443)$, although these radiances can be enhanced by the background wind-independent backscattering and by bottom reflection at $10 < Z < 15$ m at the water transparencies typical of the southern Caspian Sea. The background component vanishes when passing from the offshore and onshore radiances to their difference. Most probably, the same is true as regards the bottom reflection: to our knowledge, non-sinusoidal sand ripples are the only conceivable factor in the directional dependence of bottom reflectance, but we failed to find any evidence of such ripples in the study area. Hence, specific features of resuspension mechanisms for offshore and onshore winds determine the occurrence of the radiance loops and peaks of $dL_{\mathrm{wnav}}^{\mathrm{of\_on}}(\lambda)$ at sites with more than 10 m of water.

The resuspension mechanisms in shallows are closely associated with cross-shelf water transport, which has been subjected to intensive field experimental studies in the last 10 years (Lentz 2001, Lentz & Chapman 2004, Kirincich et al. 2005, and others). They refined earlier views going back to Ekman's theory of boundary layer dynamics. Among other things, it is acknowledged that onshore flows in the interior and bottom boundary layers along with coastal upwelling take place in order to compensate for the wind-driven offshore flow in the surface layer. As follows from

observations (Lentz & Chapman 2004, Kirincich et al. 2005), the upwelling extends seawards no more than 10 km when the bottom slope geometry is comparable to that shown in Figure 2b.

In this case, a sediment particle, just detached from the bottom by the compensation flow, starts to move shorewards in the bottom boundary layer and gradually surfaces as a result of turbulent mixing. As soon as it arrives in the surface layer, the particle moves downwind and can occur to the west of the site of detachment if particle's sinking speed is fairly slow. Under an onshore wind, the same particle moves continuously shorewards from the detachment site.

Another cause of radiance looping in the zonal profile is the fact that the bottom-to-surface distance is much shorter on the source side of the offshore wind-driven current than in the case of the onshore wind. The shorter this distance, the more probable the occurrence of a resuspended particle at the top of the layer from which the water-leaving radiance originates.

It is hardly possible to directly apply our findings to other shallows in seas and oceans because of the local specificity of this one in the Caspian Sea. Nevertheless, the pattern of a radiance loop due to equally strong winds of opposing directions appears more or less universal. This is because bottom inclination is typical of coastal shallows, and the crossing of upper and lower branches of the loop is unavoidable at the shallow's boundary where the dependence of radiance on sediments, resuspended by compensation flow, becomes negligible compared to other factors giving rise to radiance.

5. Conclusion

The wind-induced resuspension of bottom sediments is the most important factor of water-leaving radiance enhancement, inherent to marine shallows, judging in terms of the area affected by the radiance loop effect. In terms of the magnitude of the enhancement, the leading role belongs to the bottom reflectance at sites where waters are fairly transparent and the most shallow. Backscattering of resuspended particles develops at the expense of bottom reflection because a cloud of particles in the water shades the bottom. Thus, the strengthening of resuspension results in a reduced contribution of bottom reflectance into the radiance of a marine shallow. Both effects have to be accounted for when retrieving concentrations of chlorophyll, suspended matter and other constituents of shallow waters from remotely sensed radiance.

There are examples of successful accounting for bottom reflectance when retrieving the chlorophyll concentration (Cannizzaro & Carder 2006), but accounting for wind-induced resuspension is a more challenging problem. Non-averaged sea surface images of a shallow are usually rich in the

footprints of meso- and submesoscale processes, which are due to a variety of forcings and mask the manifestations of resuspension. The two-fold discrepancy between the long-term average $L_{\mathrm{wnav}}^{\mathrm{off}}(\lambda)$ and $L_{\mathrm{wnav}}^{\mathrm{on}}(\lambda)$ indicates the probability of a broader range of 'instantaneous' radiances in daily images of a shallow and gives an idea of the errors in deriving water constituents from normalized radiance without regard for the resuspension of bottom sediments. The latter is a multistage process whose stages vary temporally and spatially. This list is far from complete. To overcome these difficulties, it may be reasonable to confine the use of satellite data to images of a shallow obtained at wind speeds below 3 m s^{-1}. A comprehensive numerical model for resuspension with data assimilation capability seems to be the most appropriate solution. Further interdisciplinary studies of relevant processes and phenomena are needed to ensure the feasibility of the model approach.

Acknowledgements

References

Arfi R., Guiral D., Bouvy M., 1993, *Wind induced resuspension in a shallow tropical lagoon*, Estuar. Coast. Shelf Sci., 36 (6), 587–604, http://dx.doi.org/10.1006/ecss.1993.1036.

Booth J. G., Miller R. L., McKee B. A., Leathers R. A., 2000, *Wind-induced bottom sediment resuspension in a microtidal coastal environment*, Cont. Shelf Res., 20 (7), 785–806, http://dx.doi.org/10.1016/S0278-4343(00)00002-9.

Boss E., Zaneveld J. R., 2003, *The effect of bottom substrate on inherent optical properties: evidence of biogeochemical processes*, Limnol. Oceanogr., 48 (1, pt. 2), 346–354, http://dx.doi.org/10.4319/lo.2003.48.1_part_2.0346.

Cannizzaro J. P., Carder K. L., 2006, *Estimating chlorophyll a concentrations from remote-sensing reflectance in optically shallow waters*, Remote Sens. Environ., 101 (1), 13–24, http://dx.doi.org/10.1016/j.rse.2005.12.002.

Demers S., Terriault J.-C., Bourget E., Bah A., 1987, *Resuspension in the shallow sublittoral zone of a microtidal environment: wind influence*, Limnol. Oceanogr., 32 (2), 327–339, http://dx.doi.org/10.4319/lo.1987.32.2.0327.

Gordon H. R., 2005, *Normalized water-leaving radiance: revisiting the influence of surface roughness*, Appl. Optics, 44 (2), 241–245, http://dx.doi.org/10.1364/AO.44.000241.

Gordon H. R., McCluney W. R., 1975, *Estimation of the depth of sunlight penetration in the sea for remote sensing*, Appl. Optics, 14 (2), 413–416, http://dx.doi.org/10.1364/AO.14.000413.

Gordon H. R., Brown O. B., Evans R. H., Brown J. W., Smith R. C., Baker K. S., Clark D. K., 1988, *A semianalytic radiance model of ocean color*, J. Geophys. Res., 93 (D9), 10909–10924, http://dx.doi.org/10.1029/JD093iD09p10909.

Jerlov N. G., 1976, *Marine optics*, Elsevier, Amsterdam, 231 pp.

Karabashev G. S., Evdoshenko M. A., Sheberstov S. V., 2009, *Indication of bottom transport in shallow marine regions based on the data of satellite ocean colour scanners*, Oceanology, 49 (1), 22–30, http://dx.doi.org/10.1134/S0001437009010032.

Kopelevich O. V., Burenkov V. I., Sheberstov S. V., Shibalkova A. P., Terechova A. A., Vazyulya S. V., 2007, *Influence of the bottom reflection on balance of solar photosynthetically active radiation*, [in:] *Current problems in Optics of Natural Waters (ONW'2007)*, 4th Int. Conf. 11–15 Sept. 1993, IAP RAS, Nizhny Novgorod, 94–98.

Kirincich A. R., Barth J. A., Grantham B. A., Menge B. A., Lubchenko J., 2005, *Wind-driven inner-shelf circulation off central Oregon during summer*, J. Geophys. Res., 110, C10S03, 17 pp., http://dx.doi.org/10.1029/2004JC002611.

Lentz S. J., 2001, *The influence of stratification on the wind-driven cross-shelf circulation over the North Carolina shelf*, J. Physical Oceanography, 31 (9), 2749–2760, http://dx.doi.org/10.1175/1520-0485(2001)031<2749:TIOSOT>2.0.CO;2.

Lentz S. J., Chapman D. C., 2004, *The importance of nonlinear cross-shelf momentum flux during wind-driven coastal upwelling*, J. Phys. Oceanogr., 34 (11), 2444–2457, http://dx.doi.org/10.1175/JPO2644.1.

Mobley C. D., Sundman L. K., 2003, *Effects of optically shallow bottoms on upwelling radiances: inhomogeneous and sloping bottoms*, Limnol. Oceanogr., 48 (1, pt. 2), 329–336, http://dx.doi.org/10.4319/lo.2003.48.1_part_2.0329.

Pautov Y. V. (ed.), 1959, *Sailing directions in the Caspian Sea*, Hydrography Service, Leningrad, 274 pp., (in Russian).

Scheffer M., Portielje R., Zambrano L., 2003, *Fish facilitates wave resuspension of sediments*, Limnol. Oceanogr., 48 (5), 1920–1926, http://dx.doi.org/10.4319/lo.2003.48.5.1920.

Simonov A. I., Altman E. N., 1992, *Turbidity, transparency, and colour of the water*, [in:] *The seas of Russia. Hydrometeorology and hydrochemistry of the Seas. VI: The Caspian Sea. Issue 1: Hydrometeorological conditions*, Terziev F. S., Kosareva A. N. & A. A. Kerimova (eds.), Gidrometeoizdat, St. Petersburg, 178–186, (in Russian).